NANO LETTERS

Letter

pubs.acs.org/NanoLett

Electronic and Morphological Inhomogeneities in Pristine and Deteriorated Perovskite Photovoltaic Films

Samuel Berweger,*[,†] Gordon A. MacDonald,[†] Mengjin Yang,[‡] Kevin J. Coakley,[†] Joseph J. Berry,[‡] Kai Zhu,[‡] Frank W. DelRio,[†] Thomas M. Wallis,[†] and Pavel Kabos[†]

[†]National Institute of Standards and Technology, Boulder, Colorado 80305, United States

[‡]National Renewable Energy Laboratory, Golden, Colorado 80401, United States

Supporting Information

ABSTRACT: We perform scanning microwave microscopy (SMM) to study the spatially varying electronic properties and related morphology of pristine and degraded methylammonium lead-halide (MAPI) perovskite films fabricated under different ambient humidity. We find that higher processing humidity leads to the emergence of increased conductivity at the grain boundaries but also correlates with the appearance of resistive grains that contain PbI_2. Deteriorated films show larger and increasingly insulating grain boundaries as well as spatially localized regions of reduced conductivity within grains. These results suggest that while humidity during film fabrication primarily benefits device properties due to the passivation of traps at the grain boundaries and self-doping, it also results in the emergence of PbI_2-containing grains. We further establish that MAPI film deterioration under ambient conditions proceeds via the spatially localized breakdown of film conductivity, both at grain boundaries and within grains, due to local variations in susceptibility to deterioration. These results confirm that PbI_2 has both beneficial and adverse effects on device performance and provide new means for device optimization by revealing spatial variations in sample conductivity as well as morphological differences in resistance to sample deterioration.

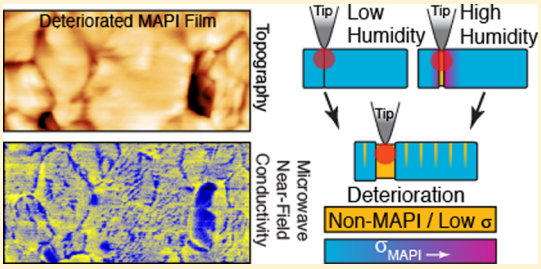

KEYWORDS: *perovskite, photovoltaic, microwave, near-field, atomic force microscope*

Much of the promise of perovskite solar cells can be attributed to the facile solution processing and the high performance metrics that appear robust to the associated morphological variations.[1] However, these morphological variations, along with the rapid deterioration of pristine films[2] and history-dependent performance,[3] present a challenge to understanding the relationship between the morphology, the electronic properties, and the resulting device performance. It therefore remains difficult to identify the structural features that govern and ultimately limit the device performance, as well as those that lead to eventual device deterioration and failure.

While there are many factors influencing device performance, the interplay of water, either atmospheric or deliberately incorporated into the precursor solution, with the $CH_3NH_3PbI_3$ (MAPI) active layer is seen to be particularly complex. On one hand, controlled H_2O exposure together with excess CH_3NH_3I (MAI) during film processing, or H_2O exposure during initial device characterization, have been shown to improve device performance[2,4,5] via both morphological improvements[6] as well as trap passivation that has been attributed to the presence of PbI_2.[7] On the other hand, ambient moisture contributes to film deterioration by several possible mechanisms that involve the formation of MAPI hydration complexes, which are strongly implicated in film breakdown through evaporation of MAI, and the subsequent buildup of residual PbI_2 as a deterioration product.[8]

The spatially inhomogeneous effects of moisture and associated PbI_2[9,10] are closely linked to grain boundaries (GBs)[7,11] but have been difficult to address directly. With the typical MAPI grain size ranging from hundreds of nanometers to a few micrometers, high-resolution techniques that are sensitive to electronic variations are thus required to discern the grain interior from the GBs. Conductive atomic force microscopy (c-AFM) in particular has been widely used to study film properties yet GB behavior has been seen to vary widely, ranging from largely insulating[12] to highly conductive,[13,14] while other results suggest improved photoconductivity[15,16] or photocurrent collection[17] at GBs. However, in addition to morphological variations between the films studied, c-AFM is highly sensitive to the surface layer and an applied c-AFM tip bias produces strong local fields that contribute to film modification and deterioration through halogen ion migration.[3,18]

Here we study local variations in sample conductivity due to morphological and compositional variations in large-grain MAPI films that yield high-efficiency photovoltaic (PV) devices[19] using scanning microwave microscopy (SMM,

Received: December 9, 2016
Revised: January 26, 2017
Published: February 2, 2017

ACS Publications © 2017 American Chemical Society

DOI: 10.1021/acs.nanolett.6b05119
Nano Lett. 2017, 17, 1796−1801

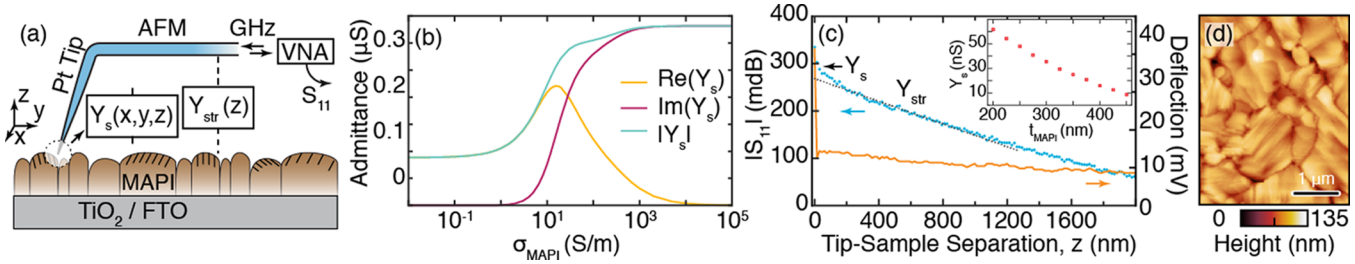

Figure 1. (a) Schematic of the experimental SMM setup. (b) Simulated tip−sample admittance Y_s as a function of sample conductivity σ_{MAPI}. (c) Approach curve showing the distance-dependent S_{11} signal together with the AFM deflection signal. Inset: MAPI thickness-dependent tip−sample admittance. (d) Contact mode AFM topography of a pristine MAPI film showing characteristic morphological features.

sometimes referred to as scanning microwave impedance microscopy, s-MIM). We develop a new approach to correct for common SMM scanning artifacts that complicate identification of the sample signal of interest. Using this artifact correction allows us to image sample conductivity variations with nanometer spatial resolution in these highly featured films, concurrent with the atomic force microscopy (AFM) topography. By systematically varying the ambient humidity during sample annealing, we find that increased humidity leads to overall higher conductivity at the GBs but also promotes the formation of isolated grains that are more insulating. Energy-dispersive X-ray spectroscopy (EDX) analysis reveals the presence of PbI_2 at these less conductive grains, suggesting that higher processing humidity leads to compositional variations. Examining highly deteriorated films, we find the GBs become wider and more insulating, and the presence of a high density of small insulating regions within grains points to the breakdown and likely fracturing of individual grains as a key pathway to advanced film degradation.

The microwave near-field microscope is based on a commercial AFM (Keysight[20]) operating in contact mode under ambient atmosphere in low-light conditions. As illustrated in Figure 1a, the microwave signal is sourced from a vector network analyzer (VNA) and delivered to the tip through a transmission line resonator. We measure the microwave signal reflected back to the VNA source (S_{11}) concurrent with the AFM topography. We use resonant modes of the transmission line near 18.7 GHz to maximize instrumental sensitivity and take advantage of higher sample mobilities.[21] As the gigahertz microwave frequency is many orders of magnitude higher than the ∼10 kHz roll-off frequency of the ionic conduction,[22,23] we do not induce halide ion migration and associated sample modification.

The S_{11} signal measured in SMM is sensitive to the tip−sample admittance (see Supporting Information), which in turn directly depends on the sample conductivity $\sigma = ne\mu$, with local carrier density n, mobility μ, and elementary charge e.[24−27] Shown in Figure 1b is the simulated[27,28] tip−sample admittance Y_s as a function of MAPI conductivity, σ_{MAPI}, showing a clear increase in Y_s with increasing σ_{MAPI}.

Several artifacts complicate identification of the sample conductivity-dependence of the S_{11} signal contribution. The most significant artifact is due to the topographic cross-talk caused by the stray tip−sample capacitance $Y_{str}(z)$[24,29] as illustrated in Figure 1a. However, for highly featured samples such as the MAPI films studied here, signal variations are also expected to result from changes in the tip−sample interaction area due to the sample curvature, as well as the sample thickness-dependent coupling of the tip to the conductive fluorine-doped tin oxide (FTO) back electrode. While $Y_{str}(z)$ can be corrected using a tip−sample approach curve,[29] the other effects are more complicated and so far have required detailed finite-element modeling to correct.[25,30] With appropriate calibrations, the real (G, conductance) and imaginary (C, capacitance) components of signal $|S_{11}| \propto Y = G + i\omega C$ can be identified.[31] However, the S_{11} signal typically drifts rapidly and renders calibrations obsolete, making quantitative scan-to-scan comparisons and thus identification of the absolute phase offset difficult. Regardless of these complications, the magnitude of the reflected microwave signal, $|S_{11}|$, gives direct information on σ_{MAPI}.[24]

In order to minimize the effect of the height-dependent stray capacitance $Y_{str}(z)$ and associated artifacts from torsional cantilever motion, we use tall high spring constant cantilevers (25Pt300A, Rocky Mountain Nanotechnology). We ensure sharp tips with radius $r < 20$ nm to maximize spatial resolution from these highly featured samples but given the inherent trade-off between tip size and signal strength this results in overall weaker signal levels. The distance-dependent S_{11} signal is shown in Figure 1c (blue dots), together with the corresponding tip deflection signal (orange line) showing the sample location. The S_{11} signal increases monotonically as the tip approaches the surface due to $Y_{str}(z)$. The S_{11} then increases sharply when the tip is near the sample, corresponding to the short-range near-field interaction at the tip apex, giving rise to Y_s. The dashed line shows the linear fit $|\hat{S}_{11}| = \alpha + \beta_1 * z$ to the distance-dependent $|S_{11}|$ signal within 1 μm of the surface. The inset to Figure 1c shows the simulated additional film-thickness dependent contribution to Y_s.

Solution-processed MAPI films exhibiting large grains were fabricated using a two-step process as previously described[19] and yield solar conversion efficiencies as high as 17%.[12] Briefly, a nonstoichiometric solution of MAI and PbI_2 (MAI/PbI_2 ratio of 1.2:1) is deposited onto a compact TiO_2 layer on fluorine-doped tin oxide (FTO). These films are then subjected to solvent bathing in an antisolvent, followed by an annealing step at ∼150 °C. To study the effect of processing moisture on morphology and electronic properties, the atmospheric water content during the grain growth annealing step was varied between 0% (N_2), 10% (dry chamber), and ∼30−45% (ambient) relative humidity (RH).

The FTO/compact TiO_2 back electrode mimics PV device architecture and ensures device-relevant morphological and associated electronic information. In order to allow humidity-induced degradation, access the sample morphology, and maximize the near-field spatial resolution, we do not encapsulate our samples. To minimize degradation, the samples are stored in the dark in an inert atmosphere and removed only

DOI: 10.1021/acs.nanolett.6b05119
Nano Lett. 2017, 17, 1796−1801

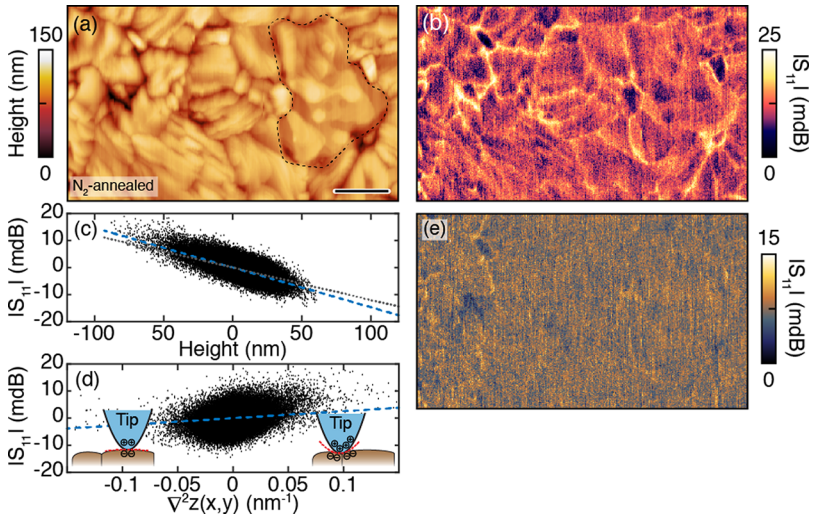

Figure 2. (a) AFM topography and (b) raw $|S_{11}|$ signal of a pristine N_2-annealedMAPI film showing a strong increase in the tip−sample admittance at the grain boundaries. (c) Height-$|S_{11}|$ and (d) $\nabla^2 z(x, y)$-$|S_{11}|$ scatterplots with predicted values (blue dashed lines) to correct topographic and curvature artifacts. Gray dotted line is stray capacitance contribution extracted from approach curve in Figure 1c. (e) Corrected $|S_{11}|$ signal from (b) showing little spatial variation in admittance, indicating uniform conductivity across sample. Scale bar: 1 μm.

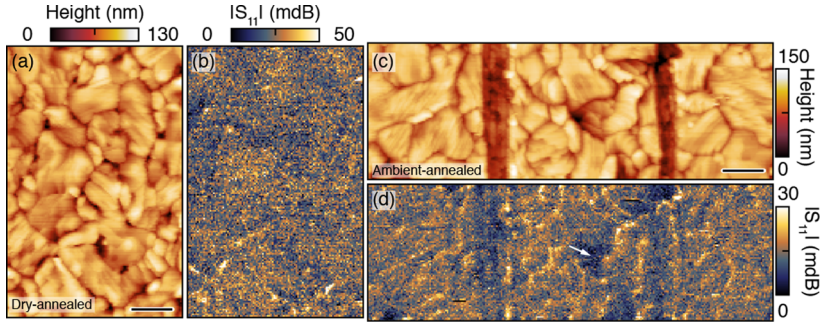

Figure 3. AFM topography and corrected $|S_{11}|$ signal, respectively, from pristine films of dry-annealed (a,b) and ambient-annealed (c,d) MAPI films. Scale bars: 1 μm.

for study where unless otherwise noted they are discarded after initial signs of degradation are seen. Signs of deterioration are typically observed 2−4 h after exposure to ambient conditions while deteriorated samples are studied after ∼12 h exposure to ambient and low-light conditions.

The contact-mode AFM topography image of a typical pristine dry-annealed MAPI film studied is shown in Figure 1d. Characteristic morphological features of the films are seen with grain boundaries clearly visible as regions of lower topography and large grains characterized by surface striations that remain uniformly oriented over individual grains but show no apparent relationship between grains. Recent results clearly suggest that grain size observed using AFM correlates well with actual size,[32] confirming that striations are features within individual grains. In addition to the large crystalline grains, smaller grains and granular structures are also visible. Nondegraded films show high repeatability in morphology and surface structure, indicative of a consolidated film.

We begin by performing SMM on pristine MAPI films under dark conditions. Shown in Figure 2 is the AFM topography (a) and the corresponding $|S_{11}|$ signal (b) of an N_2-annealed film, showing strong variations in admittance across the film with a notable increase in signal at the grain boundaries. Shown in Figure 2c is a scatterplot of AFM height and $|S_{11}|$ for each pixel in the scan. We approximate the local sample curvature by calculating the discrete Laplacian of the topography $\nabla^2 z(x, y)$ at each pixel, and generating the complementary scatterplot shown in Figure 2d. Both plots show the expected trend with increasing $|S_{11}|$ and admittance for decreasing tip−sample separation due to the stray admittance as well as the thickness-dependent Y_s contribution and for larger upward (more positive) curvature as illustrated in the inset of Figure 2d.

In order to correct for both artifacts, we assume the linear structure in the scatterplots to be due to variations in elevation and curvature, extending previous work on the topographic artifact,[29] and further supported by the approach curve in Figure 1c. We predict the contribution to $|S_{11}|$ due to these geometric effects as $|\hat{S}_{11}|(x, y) = \alpha + \beta_1 * z(x, y) + \beta_2 * \nabla^2 z(x, y)$ where the model parameters (α, β_1, and β_2) are determined by a robust method.[33] The blue dashed lines in Figure 2c,d show the predicted values. Because of the additional film thickness-dependent Y_s contribution, the predicted β_1 is larger than β_1 predicted from the approach curve in Figure 1c (gray dotted line).

The corrected S_{11} scan is shown in Figure 2e. It becomes evident that the contrast seen in the uncorrected image originates primarily from artifacts with little residual sample contrast. We conclude that the sample conductivity is highly uniform for the N_2-annealed film and serves as a reference sample, as further discussed in the Supporting Information. The

DOI: 10.1021/acs.nanolett.6b05119
Nano Lett. 2017, 17, 1796−1801

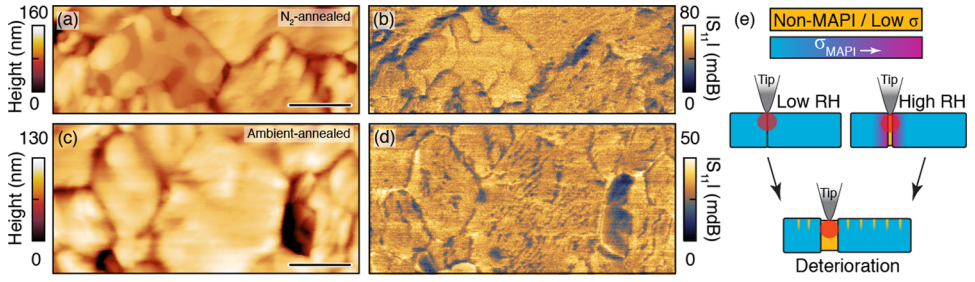

Figure 4. AFM topography and corrected S_{11} images, respectively, of deteriorated films of N_2- (a,b) and ambient-annealed (c,d) films. Scale bars: 1 μm. (e) Illustration of the observed effects of processing humidity and deterioration on the spatial accumulation of PbI_2 and associated conductivity variations. Red Circle represents the spatially confined tip near-field sampling volume.

contrast on the left side of the image is attributed to signal drift during the scan, where reduced signal levels relative to the remainder of the scan lead to a local overestimate of the scanning artifacts.

In order to further understand the relationship between processing, the resulting morphology, and the spatially varying electronic structure, we also examine pristine dry- and ambient-annealed films. Shown in Figure 3 are the AFM topography and corresponding corrected S_{11} signal, respectively, of pristine dry- (a,b) and ambient-annealed (c,d) films. Together with the N_2-annealed film in Figure 2a, we find that all pristine films studied here consist of both small grains with typical sizes 100−300 nm and irregularly shaped large grains that are >1 μm across and frequently show highly oriented striations. However, the dry-annealed films exhibit the most uniform composition of small and striated large grains, while the N_2- and ambient-annealed films show unique morphological features. The N_2-annealed film exhibits terraced flat regions not typically seen in other films, an example of which is shown enclosed in the black dashed line in Figure 2a. In contrast, the ambient-annealed film has characteristic grains that are recessed into the film, though they appear morphologically similar to other grains. The vertical cuts seen in the ambient-annealed sample are fiducial marks as further discussed in Supporting Information.

Notable differences between the films are also seen in the S_{11} images. Almost no conductivity variations are seen in the N_2-annealed sample. The dry-annealed sample similarly shows little variation in conductivity though small variations are seen between grains and at some GBs. In contrast, the ambient-annealed film shows the largest variations in electronic structure both within and across grains (we note that long-term drift prevents quantitative comparison of signal levels). Particularly notable is the reduced conductivity observed at the recessed grains, suggesting electronic differences due to compositional variations. Signal variations are also seen across grain boundaries with many showing an increased conductivity. The reduced S_{11} signal over the fiducial marks in the ambient-annealed sample indicates that the film is damaged, resulting in an overall reduced conductivity.

The increased conductivity at the GBs is likely due to the accumulation of non-MAPI species such as residual organics including MAI, or PbI_2.[34] In particular, the conductivity variations seen in SMM can be due to either p- or n-type self-doping from organics or PbI_2, respectively,[35] and cannot readily be distinguished. However, despite the excess MAI in the precursor solution, the subsequent annealing facilitates the loss of MAI and often leads to excess PbI_2,[7,19] particularly in the presence of humidity.[5] Previous work has linked the presence of PbI_2 in freshly fabricated films to improved performance via the passivation of traps, particularly near GBs,[7,9] that leads to improved carrier lifetimes[34] and associated carrier transport.[36] Similarly, the presence of moisture, which is closely linked to the interconversion between MAPI and PbI_2 via MAPI hydration complexes[8,37,38] has been shown to improve device characteristics when introduced during film processing[4,5] or early stages of PV device operation.[2]

In order to better understand the chemical composition of our films we performed EDX. Measurements from an area outside of the field of view in Figure 3d showed a I/Pb ratio of 3.02 while the dark grain indicated by the white arrow had a clearly reduced I content with a ratio of 2.63. The reduced I content indicates at least partial conversion of MAPI to PbI_2 in these grains, a conclusion further supported by spatially correlated photoluminescence (PL) mapping that shows lower emission intensity at these grains (see Supporting Information for EDX and PL data and expanded discussion). While we lack the spatial resolution to directly isolate the GBs using EDX due to the appearance of PbI_2 at higher processing humidity we consider it likely that the correlated conductivity variations at the grain boundaries arise due to the presence of PbI_2. As further discussed below, the presence of small quantities of PbI_2 localized at the GBs would lead to improved conductivity via self-doping[35] and the passivation of traps, where the resulting increased carrier lifetime is expected to increase carrier density and mobility. The local spatial averaging of the tip near-field then yields an overall higher σ_{MAPI} despite the presence of low-conductivity PbI_2. For low-humidity samples, the presence of small quantities of PbI_2 or residual organics could result in an overall increased conductivity below our sensitivity threshold while also accounting for variations in GB conductivity observed in c-AFM.[12,13,15,17] These results suggest that increasing processing humidity leads to a complex competition between the appearance of beneficial PbI_2 at GBs and the detrimental effects of grains with high non-MAPI content, explaining the diminishing benefits of high humidity levels.[5]

To further study the spatial distribution of breakdown products, we examine highly degraded films. Shown in Figure 4 is the AFM topography (a) and the corresponding corrected $|S_{11}|$ signal (b) of a heavily deteriorated N_2-annealed film. The film morphology is seen to be of reduced quality with a rougher surface and the disappearance of well-defined striations across large grains. We find an increasing prevalence of small grains in deteriorated films that indicates grain fracturing.[37] Compared to the pristine film, the GBs become highly resistive and wider in the $|S_{11}|$ image, evidence of the accumulation of reduced-conductivity material and the apparent disappearance of local trap passivation. The S_{11} image now also shows significant

DOI: 10.1021/acs.nanolett.6b05119
Nano Lett. 2017, 17, 1796−1801

variations within individual grains with well-defined but small regions of reduced conductivity giving an overall granular appearance to the film. Though these regions of reduced conductivity do not typically correlate with topographic features or those discernible in the lateral deflection signal (friction, not shown), they must originate from features at or immediately below the surface[39] within the near-field penetration depth of few tens of nanometers. One of the flat terraced regions characteristic of the N_2-annealed films is also seen, which interestingly do not typically degrade and rather maintain a uniform higher conductivity.

The degraded ambient-annealed film with the topography and corrected S_{11} signal shown in Figure 4c,d, respectively, shows very similar degradation features as the N_2-annealed film. In addition to the film roughening and the appearance of nonuniform conductivity variations, the same increase in grain boundary resistivity is also observed. The characteristic low-conductivity recessed grains are visible and also do not appear to change notably upon sample degradation. As one of the characteristic signs of sample deterioration is reduced surface stability that results in surface damage during subsequent scanning, this precludes imaging the evolution of sample deterioration through subsequent scans over the same area.[17,25]

These results indicate that deterioration leads to the accumulation of low-conductivity degradation products at spatially localized regions within as well as between grains. When the near-field probing volume confined to within tens of nanometers of the tip is increasingly composed of low-conductivity degradation products, the apparent conductivity is expected to decrease, which is in contrast to the pristine films where the small quantities of non-MAPI species act beneficially on adjacent MAPI. While we cannot definitively confirm PbI_2 as the degradation product, it is widely implicated in MAPI film failure[10,25,40] and is readily observed in our measurements to have reduced conductivity. Breakdown can occur via several different pathways[8,10,38,41] but taken together our measurements suggest two sequential steps, as illustrated in Figure 4e. First, moisture during film processing or during early operation beneficially influences GBs, which outweighs the likely negative effects of PbI_2-containing grains. Under continued exposure and possibly further aided by light, the moisture is capable of penetrating into individual grains as well as GBs, leading to deterioration that ultimately leads to reduced PV performance.[25,37]

Our measurements of pristine ambient-annealed films generally indicate a preferential accumulation of PbI_2 at the grain boundaries, while EDX measurements of the grain interiors indicate high purity MAPI. It seems likely that initial film formation involves phase segregation that leads to high purity grains and accumulation of nonstoichiometric species at the GBs as well as within unique grains. These results support recent work suggesting that PbI_2 at the GBs benefits the film morphology,[42] possibly by reducing the interfacial energy due to disorder and possible ferroelectric depolarization fields.[43] The spatially localized sample deterioration indicates strong variations in the susceptibility to film penetration by species such as water. While the increased mobility of small molecules at the disordered GBs is expected, the grain interior is more surprising. The spatially localized and weakly oriented degradation observed here within the grains raises the possibility that these variations originate in structural or crystallographic features, possibly related to surface striations. Although we cannot determine the depth profile of the degradation products, we note that deterioration along possible crystallographic features such as ferroelectric[44] or ferroelastic[45] domain walls provides a plausible mechanism for grain fracturing.[25,37] Lastly, the unique grains in the N_2-annealed films appear robust to deterioration and we cannot rule out a unique crystallographic facet[16] that is more stable under ambient conditions.

The work reported here relies on a new approach for SMM artifact correction, which has presented a long-standing problem. While calibration and careful correction of artifacts is possible,[29] instrument drift remains a problem that can render calibration obsolete over time scales as short as one scan. In this respect, using the information contained within a scan to correct artifacts is a very attractive solution as it mitigates the influence of drift and can ideally account for common sources of artifacts. The scatterplot-based approach used here is such an approach. While our linear first-order correction is only approximate, the uniform correction achieved for low-humidity samples strongly supports our approach that determines the regression model parameters simultaneously. This approach is well suited for the granular samples measured here but may not be readily applicable for more structured samples such as, for example, nanowires.[24]

We have used scanning microwave microscopy together with the concurrent AFM topography to study the effects of processing humidity and deterioration on methylammonium lead–halide perovskite film morphology and conductivity. Using a new SMM artifact correction methodology, we find increasing processing humidity leads to increased grain boundary conductivity that correlates with the appearance of less conductive grains that exhibit an increased PbI_2 content. We further find that film deterioration under ambient conditions leads to increasingly insulating grain boundaries as well as localized regions of reduced conductivity within grains. These results suggest that moisture facilitates the formation of PbI_2 but that it can lead to both beneficial or detrimental effects, depending on the phase of the film life cycle and where in the film it accumulates. Our work reveals spatial variations in film deterioration that indicate that structural or compositional inhomogeneities directly affect film susceptibility to breakdown and that improved control over film morphology could give rise to significantly improved device stability.

■ ASSOCIATED CONTENT

Supporting Information

The Supporting Information is available free of charge on the ACS Publications website at DOI: 10.1021/acs.nanolett.6b05119.

Expanded discussion of the signal origin and the artifact correction, EDX spectra, and PL maps and corresponding discussion (PDF)

■ AUTHOR INFORMATION

Corresponding Author

*E-mail: samuel.berweger@nist.gov.

ORCID

Samuel Berweger: 0000-0002-4073-5322

Notes

The authors declare no competing financial interest.

DOI: 10.1021/acs.nanolett.6b05119
Nano Lett. 2017, 17, 1796–1801

■ ACKNOWLEDGMENTS

We would like to thank Keji Lai for insightful discussions.

■ REFERENCES

(1) Sharenko, A.; Toney, M. *J. Am. Chem. Soc.* **2016**, *138*, 463.
(2) Matsumoto, F.; Vorpahl, S.; Banks, J.; Sengupta, E.; Ginger, D. *J. Phys. Chem. C* **2015**, *119*, 20810.
(3) Chen, B.; Yang, M.; Zheng, X.; Wu, C.; Li, W.; Yan, Y.; Bisquert, J.; Garcia-Belmonte, G.; Zhu, K.; Priya, S. *J. Phys. Chem. Lett.* **2015**, *6*, 4693.
(4) You, J.; Yang, Y. M.; Hong, Z.; Song, T.-B.; Meng, L.; Liu, Y.; Jiang, C.; Zhou, H.; Chang, W.-H.; Li, G.; Yang, Y. *Appl. Phys. Lett.* **2014**, *105*, 183902.
(5) Eperon, G.; Habisreutinger, S.; Leijtens, T.; Bruijnaers, B.; van Franeker, J.; DeQuilettes, D.; Pathak, S.; Sutton, R.; Grancini, G.; Ginger, D.; Janssen, R.; Petrozza, A.; Snaith, H. *ACS Nano* **2015**, *9*, 9380.
(6) Gao, H.; Bao, C.; Li, F.; Yu, T.; Yang, J.; Zhu, W.; Zhou, X.; Fu, G.; Zou, Z. *ACS Appl. Mater. Interfaces* **2015**, *7*, 9110.
(7) Chen, Q.; Zhou, H.; Song, T.-B.; Luo, S.; Hong, Z.; Duan, H.-S.; Dou, L.; Liu, Y.; Yang, Y. *Nano Lett.* **2014**, *14*, 4158.
(8) Christians, J.; Miranda Herrera, P.; Kamat, P. *J. Am. Chem. Soc.* **2015**, *137*, 1530.
(9) Wang, L.; McCleese, C.; Kovalsky, A.; Zhao, Y.; Burda, C. *J. Am. Chem. Soc.* **2014**, *136*, 12205.
(10) Merdasa, A.; Bag, M.; Tian, Y.; Källman, E.; Dobrovolsky, A.; Scheblykin, I. *J. Phys. Chem. C* **2016**, *120*, 10711.
(11) Zhang, T.; Guo, N.; Li, G.; Qian, X.; Zhao, Y. *Nano Energy* **2016**, *26*, 50.
(12) MacDonald, G.; Yang, M.; Berweger, S.; Kabos, P.; Berry, J.; Zhu, K.; DelRio, F. *Energy Environ. Sci.* **2016**, *9*, 3642.
(13) Yun, J.; Ho-Baillie, A.; Huang, S.; Woo, S.; Heo, Y.; Seidel, J.; Huang, F.; Cheng, Y.-B.; Green, M. *J. Phys. Chem. Lett.* **2015**, *6*, 875.
(14) Son, D.-Y.; Lee, J.-W.; Choi, Y.; Jang, I.-H.; Lee, S.; Yoo, P.; Shin, H.; Ahn, N.; Choi, M.; Kim, D.; Park, N.-G. *Nat. Energy* **2016**, *1*, 16081.
(15) Li, J.-J.; Ma, J.-Y.; Ge, Q.-Q.; Hu, J.-S.; Wang, D.; Wan, L.-J. *ACS Appl. Mater. Interfaces* **2015**, *7*, 28518.
(16) Leblebici, S.; Leppert, L.; Li, Y.; Reyes-Lillo, S.; Wickenburg, S.; Wong, E.; Lee, J.; Melli, M.; Ziegler, D.; Angell, D.; et al. *Nat. Energy* **2016**, *1*, 16093.
(17) Kutes, Y.; Zhou, Y.; Bosse, J.; Steffes, J.; Padture, N.; Huey, B. *Nano Lett.* **2016**, *16*, 3434.
(18) Yuan, H.; Janssen, E. D.; Naiki, H.; Steuwe, C.; Lu, G.; Moris, M.; Origu, E.; Uji-i, H.; De Schryver, F.; Samorì, P.; Hofkens, J.; Roeffaers, M. *J. Phys. Chem. Lett.* **2016**, *7*, 561.
(19) Yang, M.; Zhou, Y.; Zeng, Y.; Jiang, C.-S.; Padture, N. P.; Zhu, K. *Adv. Mater.* **2015**, *27*, 6363.
(20) Mention of commercial products is for informational purposes only, it does not imply NIST's recommendation or endorsement.
(21) Oga, H.; Saeki, A.; Ogomi, Y.; Hayase, S.; Seki, S. *J. Am. Chem. Soc.* **2014**, *136*, 13818.
(22) Lin, Q.; Armin, A.; Nagiri, R. C. R.; Burn, P. L.; Meredith, P. *Nat. Photonics* **2014**, *9*, 106.
(23) Yang, T.-Y.; Gregori, G.; Pellet, N.; Grätzel, M.; Maier, J. *Angew. Chem.* **2015**, *127*, 8016.
(24) Berweger, S.; Blanchard, P.; Blanchard, P. T.; Brubaker, M. D.; Coakley, K. J.; Sanford, N. A.; Wallis, T. M.; Bertness, K. A.; Kabos, P. *Appl. Phys. Lett.* **2016**, *108*, 073101.
(25) Chu, Z.; Yang, M.; Schulz, P.; Wu, D.; Ma, X.; Seifert, E.; Sun, L.; Zhu, K.; Li, X.; Lai, K. 2016, arXiv:1610.00755. (Accessed Oct 14, 2016).
(26) Tselev, A.; Yu, P.; Cao, Y.; Dedon, L.; Kalinin, S. V.; Maksymovych, P. *Nat. Commun.* **2016**, *7*, 11630.
(27) Lai, K.; Peng, H.; Kundhikanjana, W.; Schoen, D.; Xie, C.; Meister, S.; Cui, Y.; Kelly, M.; Shen, Z.-X. *Nano Lett.* **2009**, *9*, 1265.
(28) Berweger, S.; Weber, J. C.; John, J.; Velazquez, J. M.; Pieterick, A.; Sanford, N. A.; Davydov, A. V.; Brunschwig, B.; Lewis, N. S.; Wallis, T. M.; Kabos, P. *Nano Lett.* **2015**, *15*, 1122.
(29) Huber, H. P.; Moertelmaier, M.; Wallis, T. M.; Chiang, C. J.; Hochleitner, M.; Imtiaz, A.; Oh, Y. J.; Schilcher, K.; Dieudonne, M.; Smoliner, J.; Hinterdorfer, P.; Rosner, S. J.; Tanbakuchi, H.; Kabos, P.; Kienberger, F. *Rev. Sci. Instrum.* **2010**, *81*, 113701.
(30) Biagi, M.; Fabregas, R.; Gramse, G.; Van Der Hofstadt, M.; Juárez, A.; Kienberger, F.; Fumigalli, L.; Gomila, G. *ACS Nano* **2016**, *10*, 280.
(31) Gramse, G.; Kasper, M.; Fumigalli, L.; Gomila, G.; Hinterdorfer, P.; Kienberger, F. *Nanotechnology* **2014**, *25*, 145703.
(32) Reid, O.; Yang, M.; Kopidakis, N.; Zhu, K.; Rumbles, G. *ACS Energy Lett.* **2016**, *1*, 561.
(33) Rousseeuw, P. J.; Leroy, A. *Robust Regression and Outlier Detection*; Wiley: Hoboken, NJ, 2003.
(34) Jacobsson, T.; Correa-Baena, J.-P.; Halvani Anaraki, E.; Philippe, B.; Stranks, S.; Bouduban, M.; Tress, W.; Schenk, K.; Teuscher, J.; Moser, J.-E.; Rensmo, H.; Hagfeldt, A. *J. Am. Chem. Soc.* **2016**, *138*, 10331.
(35) Wang, Q.; Shao, Y.; Xie, H.; Lyu, L.; Liu, X.; Gao, Y.; Huang, J. *Appl. Phys. Lett.* **2014**, *105*, 163508.
(36) Hsu, H.-Y.; Ji, L.; Du, M.; Zhao, J.; Yu, E.; Bard, A. *J. Phys. Chem. C* **2016**, *120*, 19890.
(37) Li, D.; Bretschneider, S.; Bergmann, V.; Hermes, I.; Mars, J.; Klasen, A.; Lu, H.; Tremel, W.; Metzger, M.; Butt, H.-J.; Weber, S.; Berger, R. *J. Phys. Chem. C* **2016**, *120*, 6363.
(38) Yang, J.; Siempelkamp, B.; Liu, D.; Kelly, T. *ACS Nano* **2015**, *9*, 1955.
(39) Plassard, C.; Bourillot, E.; Rossignol, J.; Lacroute, Y.; Lepleux, E.; Pacheco, L.; Lesniewska, E. *Phys. Rev. B* **2011**, *83*, 121409.
(40) Liu, F.; Dong, Q.; Wong, M.; Djurisic, A.; Ng, A.; Ren, Z.; Shen, Q.; Surya, C.; Chan, W.; Wang, J.; et al. *Adv. Energy Mater.* **2016**, *6*, 1502206.
(41) Huang, W.; Manser, J.; Kamat, P.; Ptasinska, S. *Chem. Mater.* **2015**, *28*, 302.
(42) Roldán-Carmona, C.; Gratia, P.; Zimmermann, I.; Grancini, G.; Gao, P.; Nazeeruddin, M. G. M. *Energy Environ. Sci.* **2015**, *8*, 3550.
(43) Lines, M.; Glass, A. *Principles and Applications of Ferroelectric and Related Materials*; Oxford University Press: Oxford, UK, 2001.
(44) Frost, J.; Butler, K.; Brivio, F.; Hendon, C.; van Schilfgaarde, M.; Walsh, A. *Nano Lett.* **2014**, *14*, 2584.
(45) Hermes, I.; Bretschneider, S.; Bergmann, V.; Li, D.; Klasen, A.; Mars, J.; Tremel, W.; Laquai, F.; Butt, H.-J.; Metzger, M.; Berger, R.; Rodriguez, B.; Weber, S. *J. Phys. Chem. C* **2016**, *120*, 5724.

DOI: 10.1021/acs.nanolett.6b05119
Nano Lett. 2017, 17, 1796−1801